RSC Advances

ROYAL SOCIETY OF CHEMISTRY

www.rsc.org/advances

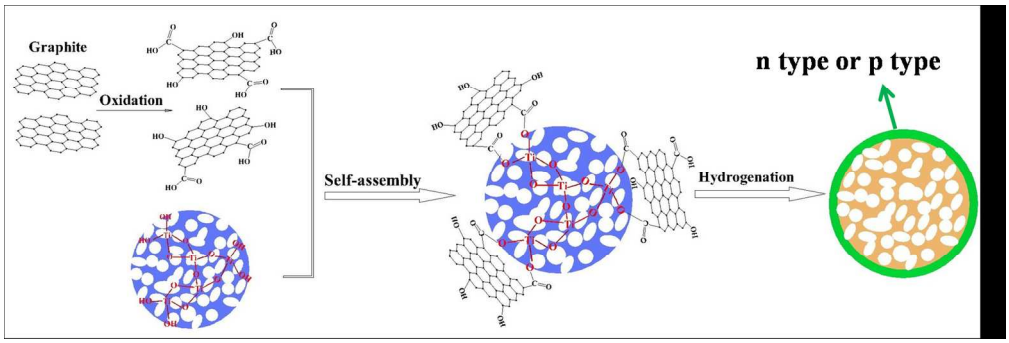

The preparation processes of the hydrogenated TiO2@reduced graphene oxide composites with p-n heterojunctions.
307x102mm (150 x 150 DPI)

The Enhanced Photoactivity of Hydrogenated TiO_2 @ Reduced Graphene Oxide with p-n Junctions

Xiaoying Zhang and Zhuoyuan Chen*

The hydrogenation of graphene oxide (GO)-TiO_2 composites with quasi-shell-core structure was performed in the temperatures range of 250-550 ˚C. All the synthetic hybrid materials displayed enhanced photocatalytic performances and the highest photoactivity was obtained by the hybrid material prepared at 450 ˚C due to the formation of p-n junction and appropriate charge mobility. The semiconductor behaviour of the resultant reduced graphene oxide (RGO) in the composites had a crossover from p-type to n-type when the hydrogenated temperature increased from 450 ˚C to 550 ˚C.

1. Introduction

Graphene and its derivatives have recently attracted extensive attention as potential candidates for the efficient composite photocatalysts because of their exceptional specific surface area, fascinating charge carrier mobility and high transparency.[1-3] In graphene, the sp^2 hybrid carbon atoms bond together to form the hexagonal framework, and the remained p orbital of each carbon atom overlaps to produce a fully occupied π bond known as the valence band and an empty π^* bond called the conduction band.[4] The valence band and the conduction band touch at the Brillouin zone corners, therefore graphene displays an ambipolar electric field effect, and the semiconductor behaviour type and concentration of its charge carriers can be tuned by electrical and/or chemical modification.[5,6] It is well known that controlled oxidation of graphene (or partial reduction of graphene oxide (GO)) can modify the electronic band structure of graphene, open up an energy gap between the valence bands and the conduction bands and therefore transform the semiconductor behaviour type to either p-type or n-type.[7-9] Furthermore, the value of the energy gap has a correlation with the reduction degree of GO.[10,11] Therefore, GO with different reduction degrees would give rise to a diverse energy gap and semiconductor behaviour type, resulting in different chemical properties of GO. The rational design of graphene-based photocatalysts has led many theoretical and experimental efforts worldwide. In these photocatalysts, graphene is usually prepared by the reduction of GO (commonly referred as RGO), because GO provides abundant anchoring sites to bind efficiently with semiconductor or metal nanoparticles.

Recently, there have been several reports highlighting the improvements in photocatalytic activity of TiO_2 nanoparticle combined with RGO for the degradation of organic molecules and photocatalytic splitting of water.[12-17] Most of the RGO-TiO_2 composite photocatalysts reported previously, RGO is an n-type semiconductor and considered as transmission medium for charge transport and subsequent charge separation.[12-16] More recently, Chen et al. fabricated GO-TiO_2 composites with different concentration of GO and TiO_2 nanoparticles.[17] They found that the semiconductor behaviour of GO in those composites depended on its concentration, because the variation of stress could be caused by the growth of TiO_2 nanocrystals on the GO surface. However, GO suffers from low conductivity. This problem can be solved by a partial reduction.

In addition, for improving the photocatalytic performance of RGO-TiO_2 composites, it is of great importance to form maximum interfacial contact between TiO_2 and RGO. However, the TiO_2 nanoparticles tend to agglomerate and have poor point contact with the RGO surface. To address this issue, the hierarchical micro/nano-structure mesoporous spheres may be a favourable candidate, which can simultaneously offer abundant catalytic active sites, excellent light-scattering characteristics and a highly conductive pathway for charge carriers collection.[18] Our recent work revealed that the photoelectrochemical performances of TiO_2 mesoporous spheres can be further enhanced by hydrogenation, because the hydrogenation not only boosts the light absorption but also improves the electrical conductivities of TiO_2.[18]

Herein, the hybrids of RGO and hydrogenated TiO_2 mesoporous spheres (RGO-HMT) with quasi-shell-core structure were synthesized by the hydrogenation of graphene oxide (GO)-TiO_2 composites at different temperatures. In these composites, either p-type or n-type semiconductor behaviour has been observed for RGO with diverse reduction degrees. The effect of the semiconductor behaviour type on photoelectronic and photocatalytic activity of RGO-HMT composites has also been studied in detail.

2. Experimental

2.1 Synthesis of reduced graphene oxide-hydrogenated micro/nano-TiO_2 spheres (RGO-HMT)

GO was firstly prepared using graphite powder (Aldrich, powder, <20 micron, synthetic) according to the previous literature reported by Hummers with minor revision.[19] The hierarchical micro/nano-TiO_2 spheres (denoted as MT) were then synthesized as described in our previous work without any variation.[18] In brief, 2 mL tetrabutoxytitanium was added to 50 mL ethylene glycol, magnetically stirring for 8 h at room temperature. The mixture was then poured into a solution containing 170 mL acetone and 2.7 mL water, stirring vigorously. And then the white precipitate was obtained by centrifugation, followed by washing with ethanol for five times and was dried at 50 °C. After reflux

and centrifugation, the white powders were calcined in air at 500 °C for 2 h to improve their crystallization and obtain the MT samples. Finally, the GO-TiO_2 spheres composite (denoted as GO-MT) was obtained by the self-assembled method, described in the literature.[20] 0.5 g MT was dispersed in water with ultrasonication, and then a 1 wt% amount of GO was added to the above solution. The mixture was aged with vigorous stirring for overnight. Then, this mixture was filtered and washed several times with 1 M HCl aqueous solution containing 1% H_2O_2 and deionized water to remove impurities. Prior to hydrogenation, the obtained GO-MT powders were then dried at 60 ˚C for 4 h in a vacuum oven. The hydrogenation was performed as follows: The as-prepared GO-MT samples were transferred to a quartz boat located at the center of a quartz tube, which was horizontally placed in a tubular furnace. Before starting the heat treatment, the inner tube of the furnace was evacuated and purged with nitrogen and these two steps were repeated four times. After this, the inner tube was evacuated and purged with hydrogen, and these were repeated twice. Finally, the powders were annealed at 250-650 ˚C for 2 h with 5 °C min^{-1} under 20 bar H_2. After being cooled to room temperature, the reduced graphene oxide-hydrogenated micro/nano-TiO_2 spheres T (RGO-HMT T) were obtained, where T stood for the hydrogenated temperature. For comparison, MT was also hydrogenated at 450 ˚C to obtain hydrogenated MT (HMT).

2.2 Physical property characterization

The morphologies and the microstructures of the synthetic products were investigated using field emission scanning electron microscopy (FESEM, HITACHI S-4800) and a high-resolution transmission electron microscope (HRTEM, FEI Tecnai G20, FEI Company, USA). Their crystalline structures and bonding information were analyzed using X-ray diffraction (XRD, D/MAX-2500/PC; Rigaku Co., Tokyo, Japan) and the optical absorption properties were recorded in the wavelength range of 200-800 nm by using a Hitachi U4100 spectrophotometer equipped with an integrating sphere.

2.3 Photocatalytic degradation Rhodamine B (RhB)

The photocatalytic degradation measurements were performed under illumination with a 300 W Xenon lamp (PLS-SXE300, Beijing Changtuo Co. Ltd., Beijing, China). 0.1 g prepared samples were mixed with an aqueous RhB solution (100mL, 10 mg·L-1) and were stirred vigorously in the dark for 30 min to achieve an adsorption-desorption equilibrium. This mixture was then placed under a 300 W Xenon lamp and 3 mL suspension was withdrawn at regular intervals and stored in the dark. After the completion of the test, these suspensions were centrifuged at 10,000 rpm for 10 min to remove suspended particles, and the concentration of RhB was determined.

2.4 Photoelectrode preparation

The prepared powder samples were fabricated into photoelectrodes as follows: 0.01 g the obtained powder was added to 0.1 mL deionized water in an agate mortar, and then carefully ground for 10 min, resulting in a homogeneous paste. This paste was evenly overlaid onto the conductive side of the pre-cleaned fluorine-doped tin oxide glass substrate, followed by heat drying at 120 ˚C for 2 h under vacuum condition. A copper wire was then connected to the conductive side of the fluorine-doped tin oxide glass using conductive silver tape. The substrate edges and the metal contact region were sealed with insulating epoxy resin after the conductive silver tape had dried. The working electrode area is 0.8 cm2.

2.5 Photoelectrochemical measurements

The photoelectrochemical and electrochemical measurements were performed by an Electrochemical Workstation (CHI660D, Shanghai Chenhua Instrument Co., Ltd., Shanghai, China) in a three-electrode cell with the obtained photoelectrode as work electrode, Pt foil as counter electrode and Ag/AgCl electrode (saturated KCl) as reference electrode. A 300 W Xenon lamp (PLS-SXE300, Beijing Changtuo Co. Ltd., Beijing, China) was used as the light source. The electrolyte used was 0.5 M Na_2SO_4 solution (pH=7). The i-t curves were measured under white light and visible light irradiation at different bias voltages. The electrochemical impedance spectroscopy (EIS) experiments were conducted in the dark. The frequency range was chosen from 100 kHz to 1 Hz with an AC modulation signal of 5 mV at a dc potential of 0 V vs Ag/AgCl electrode. The EIS results were analyzed using a Zsimpwin software.

3. Results and Discussion

3.1 The structural characterizations of as-prepared RGO-HMT composites

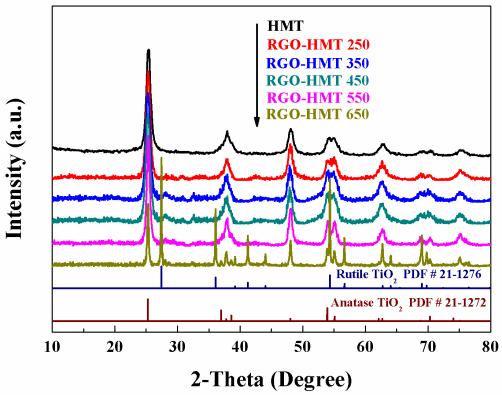

Fig. 1 XRD patterns of the as-synthesized HMT and RGO-HMT composites with five different temperatures from 250 to 650 ˚C. Standard diffraction peaks of anatase TiO_2 (JCPDS *No.* 21-1272) and rutile TiO_2 (JCPDS *No.* 21-1276) are shown as vertical bars.

XRD patterns of HMT and a series of RGO-HMT composites (RGO-HMT 250, RGO-HMT 350, RGO-HMT 450, RGO-HMT 550 and RGO-HMT 650) were recorded to confirm their crystallographic phases and the relevant results were presented in Fig. 1. Except RGO-HMT 650, the RGO-HMT composites exhibit similar diffraction peaks to HMT and all the diffraction peaks can be satisfactorily indexed to the anatase TiO_2 (JCPDS *No.* 21–1272). No significant characteristic diffraction peaks corresponding to RGO or GO can be detected for all RGO-HMT composites. This is presumably caused by the little amount of RGO in the composites. However, the RGO-HMT 650 has a

different crystalline form. RGO-HMT 650 is comprised of anatase and rutile phase structure of TiO_2. As for RGO-HMT 650, the characteristic peaks observed at 25.3°, 37.8°, 48.0°, 53.9° and 55.1° can be attributed to the diffractions of the (101), (004), (200), (105) and (211) crystal planes of anatase TiO_2, respectively. While the diffraction peaks located at 27.4°, 36.1°, 41.2°, 44.1°, 54.3° and 56.6° can be assigned to the (110), (101), (111), (210), (211) and (220) faces of rutile TiO_2. It means that the crystalline phase transformation from anatase to rutile occurs when the hydrogenated temperature reaches 650 ˚C. In the following, the RGO-HMT composites with anatase phase TiO_2 hydrogenated below 550 ˚C are intensively studied and discussed.

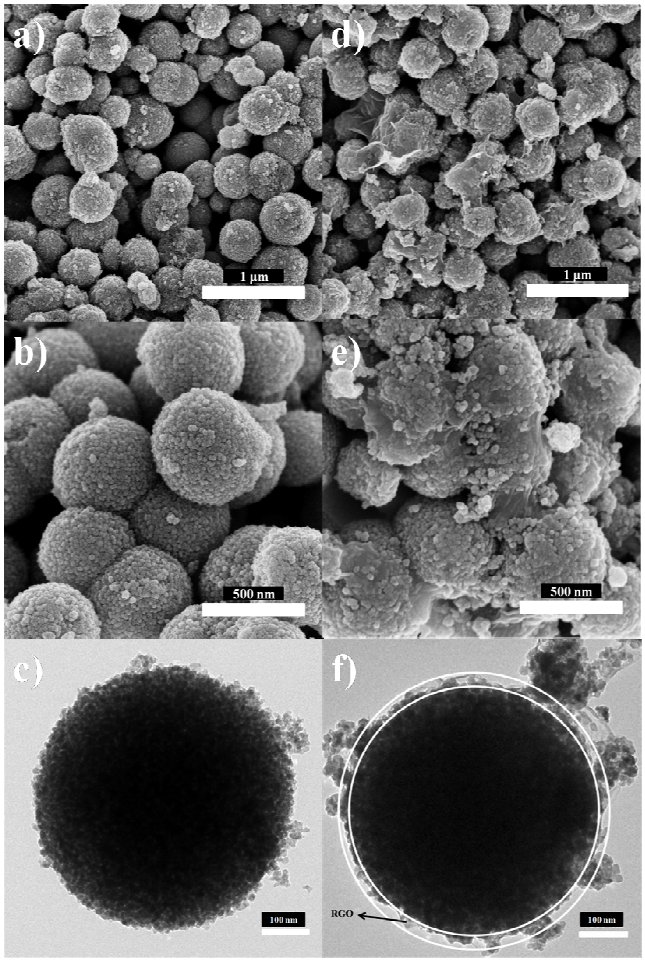

Fig. 2 Typical SEM images (a and b) and TEM image (c) of HMT samples; Low-magnification SEM image (d), high-magnification SEM image (e) and TEM (f) image of the as-prepared RGO-HMT 450.

The microscopic morphology and crystal structure of the obtained RGO-HMT were characterized by SEM, TEM and HRTEM. Fig. 2a and Fig. 2b present the SEM images of the as-prepared HMT with different magnifications. Typical SEM image (Fig. 2a) at low magnification describes that the HMT samples are highly homogeneous spherical particles with a diameter of 500-550 nm. From the high-magnification SEM image (Fig. 2b), it can be clearly seen that the surface of the pure HMT spheres is rough, and the spheres are composed of large numbers of TiO_2 nanoparticles. By contrast, the surface of the RGO-HMT is wrapped in a typical crinkly and rippled layer, which is believed to be RGO nanosheets (Fig 2d and Fig. 2e). Compared with the TEM images of HMT (Fig. 2c), further observations of RGO-HMT (Fig. 2f) exhibit a curved characteristic and a low contrast for the wrinkle-like RGO nanosheets, revealing that the quasi-shell-core structure is successfully formed. The compact interconnection between HMT core and RGO shell is believed to be helpful for charge transfer between them.

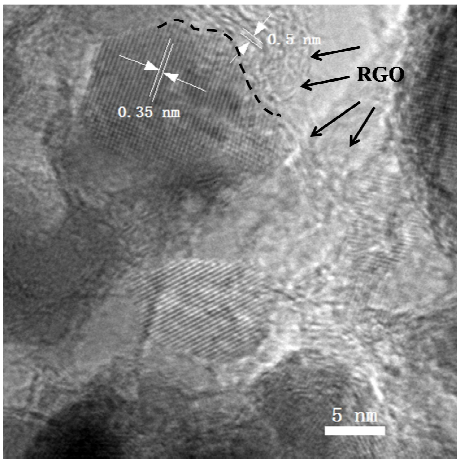

Fig. 3 HRTEM images of the as-prepared RGO-HMT 450.

In the HRTEM image (Fig. 3), the lattice fringes with d spacing of 0.35 nm can be well indexed to the (101) crystal plane of anatase TiO_2, which confirms that the core of as-prepared RGO-HMT is highly crystallized. A different kind of lattice fringes with d spacing of 0.5 nm can be found in the shell region, which corresponds to the typical (002) interlayer-stacking distance of RGO.[21,22] This value is larger than the interlayer spacing of pristine graphite (0.34 nm) but smaller than that of GO (1 nm).[23,24] It is implied that the oxygen containing functional groups on GO has been partially removed and GO is transformed into RGO during the hydrogenation[25].

3.2. Photocatalytic activity of RGO-HMT composites

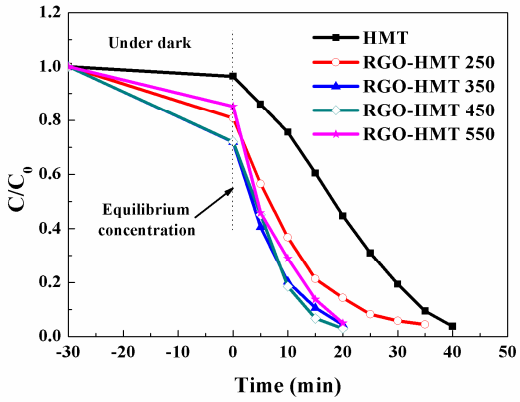

Fig. 4 Photocatalytic activities of obtained HMT and RGO-HMT samples for degradation of RhB under simulated solar illumination. C and C_0 are

the RhB concentration after photocatalytic degradation and the initial concentration of RhB aqueous solution (10 mg L^{-1}), respectively.

The photocatalytic activity of the prepared RGO-HMT composites was evaluated by photocatalytic degradation of RhB at room temperature. For comparison, the photocatalytic performance of HMT photocatalyst had also been investigated. Fig. 4 plots the relative changes in the concentration of RhB aqueous solution as a function of the reaction time. Before exposed to light, the photocatalysts were mixed with RhB under dark conditions and stirred for 30 min to achieve the adsorption–desorption equilibrium. It can be seen from Fig. 4, the RhB equilibrium concentrations of RGO-HMT composites are all much lower than that of pure HMT sample, indicating that the as-prepared RGO-HMT composites exhibit remarkably enhanced absorption capacity for RhB. That may be reasonably due to the high surface area of RGO nanosheets and their prominent affinity toward aromatic molecules.[26] Benefited from such high absorption capacity, RGO-HMT composites are expected to exhibit an excellent photocatalytic activity for the degradation of RhB, since the absorption of the reactant is positively related with the latter photocatalytic degradation reaction on the surface of the photocatalyst.[27] It takes 40 min for the HMT photocatalyst to finish the degradation of almost all the RhB dye, while the corresponding photo-degradation time is 35 min for RGO-HMT 250 and less than 20 min for RGO-HMT 350, RGO-HMT 450 and RGO-HMT 550. It is a remarkable fact that the photocatalytic activity of composites increases gradually with the temperature up to 450 ˚C and it does not enhance with the further increase of hydrogenated temperature. Therefore, it is evident that the photocatalytic activity is strongly dependent on the hydrogenated temperature of the RGO-HMT composites.

3.3. Reasons for the high photocatalytic activity of RGO-HMT composites

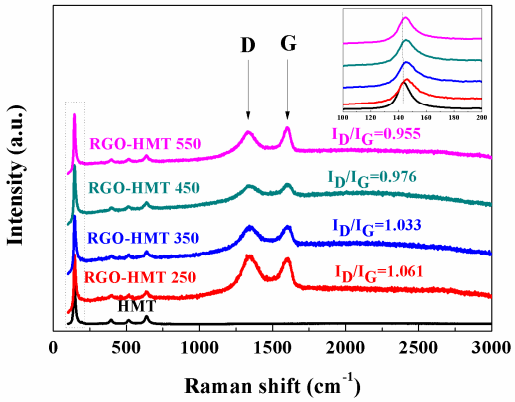

Fig.5 Raman spectra of RGO-HMT and HMT.

In order to clarify the possible reasons for the enhanced photoelectrochemical performances of RGO-HMT composites, their structural and optical properties have been studied. Further insights of the structural properties of RGO-HMT were characterized from Raman spectroscopy. Fig. 5 displays the Raman spectra of HMT and RGO-HMT composites. For HMT, the peaks at 144 cm^{-1} (E_g), 399 cm^{-1} (B_{1g}), 513 cm^{-1} (A_{1g}) and 639 (Eg) cm^{-1} are attributed to Raman modes of anatase TiO_2,[28] which is in accord with the XRD results. As well as the anatase peaks of TiO_2, two distinctive D and G bands at 1342 cm^{-1} and 1612 cm^{-1} with different relative intensities (I_D/I_G) are observed in all the RGO-HMT composites. I_D/I_G is an index of the relative concentration of sp^3 defects compared to the sp^2 graphene domains. As shown in Fig. 5, the values of I_D/I_G ratio are in the order of RGO-HMT 250 (1.061) > RGO-HMT 350 (1.033) > RGO-HMT 450 (0.976) > RGO-HMT 550 (0.955). It indicates that part GO is reduced and more graphitization of RGO-HMT is obtained with the increase of the hydrogenated temperature, which is positively correlated with the electron migration ability.[29,30] In addition, the shift of the E_g mode at 144 cm^{-1} towards a higher wavenumber (146 cm^{-1}) is detected in RGO-HMT composites, which implies the formation of Ti-O-C bonds on the surface of anatase TiO_2 due to the introduction of RGO.[31]

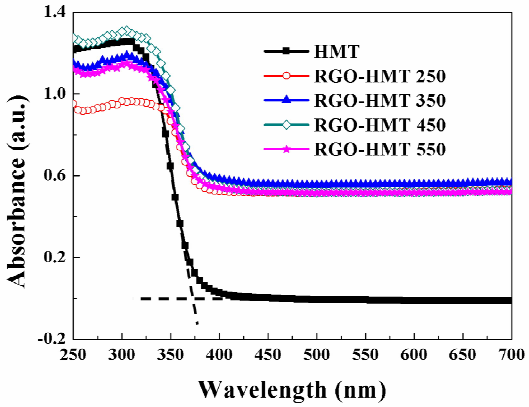

Fig. 6 UV/Vis diffuse reflectance spectra of the prepared HMT and RGO-HMT samples with different temperatures.

The optical properties of the as-synthesized HMT and RGO-HMT composites hydrogenated at different temperatures were measured via UV/Vis diffuse reflectance spectra and compared in Fig. 6. HMT exhibits a typical semiconductor absorption property of TiO_2, which has a strong absorption in the ultraviolet region and almost no absorption in the visible light region. By contrast, the background absorption of RGO-HMT composites is remarkably enhanced in the visible light region. Such large background absorption has also been observed in previous researches regarding graphene-semiconductor photocatalysts, which is attributed to the absence of a well defined band gap of graphene.[32] Furthermore, the light absorption threshold of HMT is approximately 375 nm, which is distinguished by extrapolating the steep slopes in the curve to the long wavelength side. Compared with that of HMT, red shift to higher wavelength is observed in the absorption edge of the RGO-HMT nanocomposites. The red shift of the absorption onsets results from the Ti–O–C bond formed through the interactions between RGO and HMT, favorable to the charge transfer**.** The results are consistent with the previous reports.[33,34]

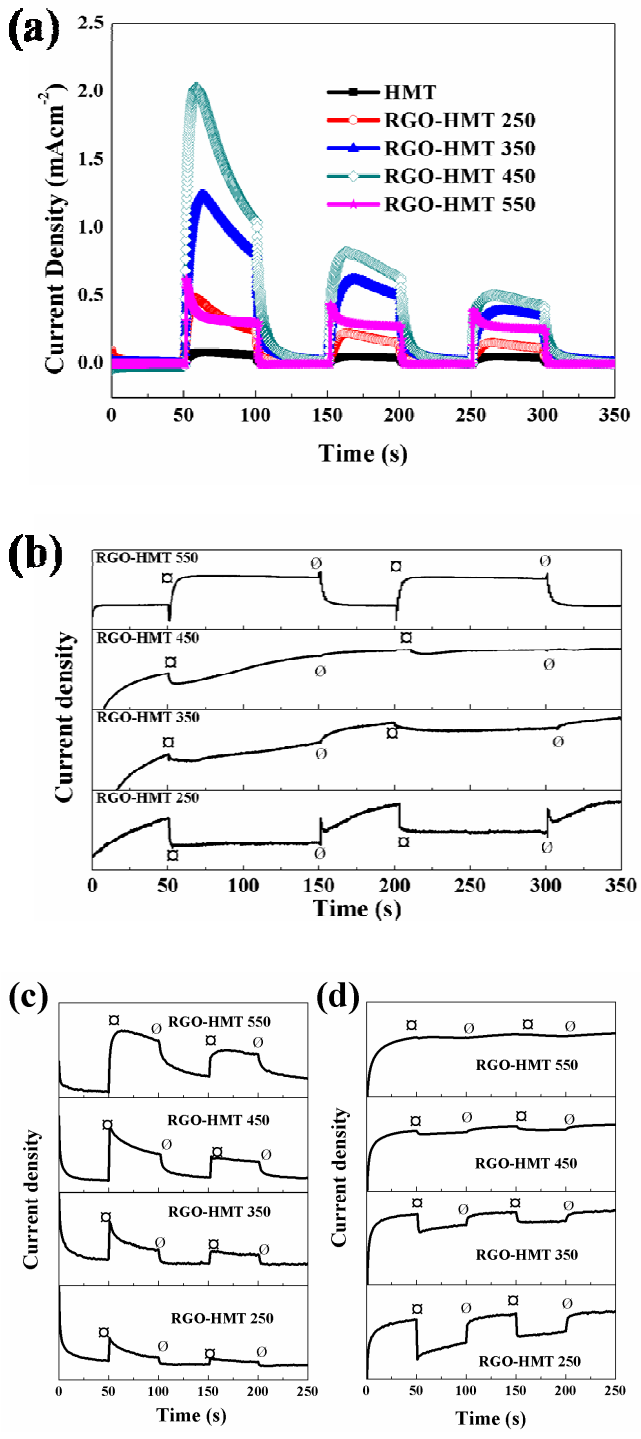

Fig. 7 Time-dependent profiles of photocurrent responses (i-t curves) collected in 0.5 M $NaSO_4$ solution with simulated solar light at a constant bias voltage of 0 V (*vs.* Ag/AgCl) (a) and visible light irradiation (λ> 420 nm) at a bias voltage of 0 V (*vs.* Ag/AgCl) (b), 0.5 V (*vs.* Ag/AgCl) (c) and -0.5 V (*vs.* Ag/AgCl) (d) switched on and off.

Photoinduced charge separation in the photocatalysts was evaluated by carrying out the transient photocurrent response. Fig. 7a and Fig. 7b present the photocurrent densities versus time curves for the samples coated photoelectrodes measured at a fixed bias potential of 0 V vs. Ag/AgCl with several on-off cycles of simulated solar light irradiation and visible light illumination (λ> 420 nm), respectively. The transient photocurrent of RGO-HMT composites electrode with a simulated solar light pulse of 50 s is shown in Fig. 7a. It is noted that, the photocurrent density of the RGO-HMT 450 composite photoelectrode (more than 0.8 mA cm^{-2}) is 4 times larger than that of HMT (less than 0.2 mA cm^{-2}), confirming the high efficiency of RGO on suppression of photogenerated electron–hole recombination in HMT.[35] Generally, the better the conductivity of RGO is, the higher the charge separation efficiency is.[12-16] In association with our Raman analysis (Fig. 5), the order of electron transfer rate of RGO in RGO-HMT composites is RGO-HMT 550> RGO-HMT 450> RGO-HMT 350> RGO-HMT 250. However, the order of the photocurrent responses is as follows: RGO-HMT 450> RGO-HMT 350> RGO-HMT 550> RGO-HMT 250.

In order to clarify the possible reasons for the issues mentioned above, transient photocurrents of RGO-HMT under visible light (wavelength longer than 420 nm) illumination have been analyzed (Fig.7 b, c, d and Fig. S1). According to UV/Vis diffuse reflectance spectra analysis, the absorption of RGO-HMT composites above 420 nm is resulting from the absorption of the RGO (Fig. 6). Therefore, the i-t curve under the visible light is a key reflex for the photo response of RGO. It can be seen in Fig. 7b, the RGO-HMT 250, RGO-HMT 350 and RGO-HMT 450 possess a cathodic photocurrent, which is a p-type photoresponse.[17,36] While, RGO-HMT 550 possesses an anodic photocurrent, which means an n-type photoresponse.[17,36] This phenomenon suggests different kinds of semiconductor behaviour types of RGO are existed in RGO-HMT composites. When the irradiation wavelength extended to the white light region (Fig. 7a), photocurrent conversion from cathodic to anodic was found for RGO-HMT 250, RGO-HMT 350, and RGO-HMT 450, but no photocurrent conversion was found for RGO-HMT 550. Wavelength dependent photocurrent conversion of RGO-HMT 250, RGO-HMT 350 and RGO-HMT 450 suggests the formation of a p-n heterojunction.[17,36] According to previous work, the existence of p-n heterojunctions in RGO-HMT composites can also be studied by the I-t characteristics at different bias voltages.[17,36] Fig.7c, Fig. 7d and Fig. S1 identify the I-t characteristics of RGO-HMT hybrids under visible light irradiation at a bias voltage of 0.5 V and -0.5 V (*vs.* Ag/AgCl), respectively. In the case of RGO-HMT 550 and RGO-HMT 650, there is no photocurrent direction conversion when the electrode potential ranges from 0.5 V to -0.5 V (*vs.* Ag/AgCl). By contrast, for RGO-HMT 250, RGO-HMT 350 and RGO-HMT 450, the current is in forward direction as the electrode potential is 0.5 V (*vs.* Ag/AgCl), whereas the current in the reverse direction is observed at -0.5 V (*vs.* Ag/AgCl). This photocurrent direction conversion phenomenon corroborates the existence of p-n heterojunctions in RGO-HMT 250, RGO-HMT 350 and RGO-HMT 450 again[17,36].When a p-type RGO is in contact with an n-type HMT, the electric fields are built at the interfaces between RGO and HMT, and the direction of the electric field is pointed from the HMT to the RGO. The existence of these inner electric fields can significantly increase the separation efficiency of the photogenerated electron–hole pairs.

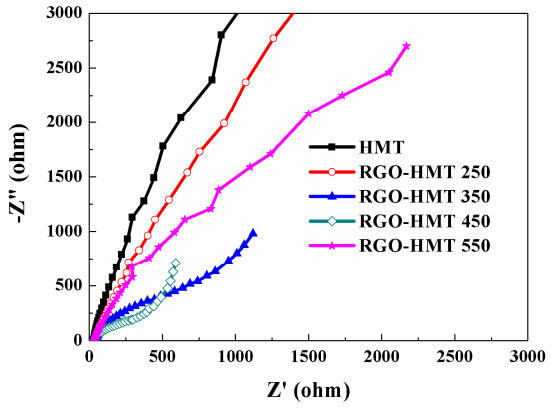

Fig. 8 Expanded range of EIS for HMT and RGO-HMT samples with different temperatures in Nyquist plots in 0.5 M $NaSO_4$ under dark at a dc potential of 0 V *vs.* Ag/AgCl with an ac potential of 5 mV between frequency range from 100 kHz to 1 Hz.

EIS is a useful tool to study the electron migration ability and the interface electron transfer, which are closely related to the photoelectrochemical performance of semiconductor materials. In this work, the impedance values of the photoanode were measured in 0.5 M Na_2SO_4 electrolyte in the dark, as shown in Fig. 8 and Fig. S2. For HMT, RGO-HMT 250 and RGO-HMT 550 represent an incomplete semicircle in the Nyquist plots and a broad and asymmetric peak in the Bode plots, suggesting at least two time constants present in the frequency range between 1 Hz and 100 kHz. In contrast, RGO-HMT 350 and RGO-HMT 450 exhibit two semicircles in the Nyquist plots or two characteristic frequency peaks in the Bode plots. Although the shapes of the impedance for RGO-HMT composites are different, there are two time constants for all the composites. The semicircle in high frequency regions is assigned to the electron transport between the particles, and the one in the low frequency region corresponds to the charge transfer at the electrode/electrolyte interface. [37] The impedances of all the RGO-HMT composite photoanodes are lower than that of HMT photoanode at the same frequency, especially in the high frequency regions. It is indicated that the introducing of RGO will facilitate the electrons transfer. However, the promotion mechanism may be different. As mentioned above, there is a p-n heterojunction between RGO and HMT for the RGO-HMT 250, GO-HMT 350 and RGO-HMT 450 samples, which is beneficial for the separation efficiency of the photoexcited electrons and holes.[38] Although such a p-n heterojunction exists in RGO-HMT 250 and RGO-HMT 350, their electron transfer resistance is still large, due to the quite low conductivity of these prepared RGO (based on Raman spectra, Fig. 5). Nevertheless, in the case of RGO-HMT 550, the semiconductor behaviour types of RGO is n-type. The superior separation efficiency of RGO-HMT 550 might be due to the suitable work function and the high electrical conductivity of RGO. Since the work function of RGO is more positive than the conduction band of TiO_2, the photogenerated electrons tend to transfer from the TiO_2 conduction band to RGO. [39] On the other hand, the RGO has unexpectedly excellent conductivity due to its two dimensional structure, which enables an effective charge transfer. The results of EIS are in good agreement with the above i-t tests. These results confirmed that all the synthetic hybrid materials displayed enhanced photocatalytic performances and the highest photoactivity was obtained by the hybrid material prepared at 450 ˚C due to the formation of p-n junction and appropriate charge mobility.

.

4. Conclusion

We fabricated RGO-HMT composites with self-assembled quasi-shell-core structure at different hydrogenated temperatures and tested their photocatalytic activities. All the synthesized composites showed enhanced photocatalytic performances. The resultant RGO in the composites is a p-type semiconductor when the hydrogenated temperature is lower than 450 ˚C and it converses to an n-type semiconductor with the temperature higher than 450 ˚C. Despite the low charge mobility, a p-n junction is built in the composites with the hydrogenated temperature below 450 ˚C, promoting the separation efficiency of photogenerated electron–hole pairs. Although there is not p-n junction in RGO-HMT 550, its photoactiviy has an improvement to some extent, due to the excellent conductivity of the dimensional planar structure of the RGO. Benefited from the formation of p-n junction and appropriate charge mobility, the hybrid material prepared at 450 ˚C yields the highest photocatalytic performance.

Acknowledgements

This work was financially supported by the National Natural Science Foundation of China (41376126), Hundreds-Talent Program of the Chinese Academy of Sciences (Y02616101L), China Postdoctoral Science Foundation (2014M551968) and Postdoctoral Innovation Project of Shandong Province (201402041).

Notes and references

Key Laboratory of Marine Environmental Corrosion and Bio-fouling, Institute of Oceanology, Chinese Academy of Sciences, 7 Nanhai Road, Qingdao 266071, China; Fax: +86-532-82880498; Tel: +86-532-82898731;

**Corresponding author, Prof. Zhuoyuan Chen;*

Email: zychen@qdio.ac.cn;

† Electronic Supplementary Information (ESI) available: [details of the i-t curves of RGO-HMT 650 were studied at different bias voltage of 0 V, 0.5 V and -0.5 V (*vs.* Ag/AgCl) under visible light irradiation; Full range of impedance spectra of HMT and RGO-HMT samples with different temperatures and Equivalent circuit modelvfor EIS should be included here]. See DOI: 10.1039/b000000x/

1. B. Li, X. Zhang, X. Li, L. Wang, R. Han, B. Liu, W. Zheng, X. Li and Y. Liu, *Chem. Commun.*, 2010, **46**, 3499.
2. X. Cao, G. Tian, Y. Chen, J. Zhou, W. Zhou, C. Tian and H. Fu, *J. Mater. Chem. A*, 2014, **2**, 4366
3. B. Guo, Q. Liu, E. Chen, H. Zhu, L. Fang and J. R. Gong, *Nano Lett.*, 2010, **10**, 4975.
4. C. Berger, Z. Song, X. Li, X. Wu, N. Brown, C. Naud, D. Mayou, T. Li, J. Hass and A. N. Marchenkov, *Science*, 2006, **312**, 1191.
5. Y. Zhu, S. Murali, W. Cai, X. Li, J. W. Suk, J. R. Potts and R. S. Ruoff, *Adv. Mater.*, 2010, **22**, 3906.
6. H. Liu, Y. Liu and D. Zhu, *J. Mater. Chem.*, 2011, **21**, 3335.
7. H. Sojoudi, J. Baltazar, L. M. Tolbert, C. L. Henderson and S. Graham, *ACS Appl. Mater. Interfaces*, 2012, **4**, 4781.

8. S. Sutar, E. S. Comfort, J. Liu, T. Taniguchi, K. Watanabe and J. U. Lee, *Nano Lett.*, 2012, **12**, 4460.
9. J. Baltazar, H. Sojoudi, S. A. Paniagua, J. Kowalik, S. R. Marder, L. M. Tolbert, S. Graham and C. L. Henderson, *J. Phys. Chem. C*, 2012, **116**, 19095.
10. D. W. Boukhvalov and M. I. Katsnelson, *J. Am. Chem. Soc.*, 2008, **130**, 10697.
11. P. Duy-Thach and G.-S. Chung, *J. Phys. Chem. Solids*, 2013, **74**, 1509.
12. E. Lee, J.-Y. Hong, H. Kang and J. Jang, *J. Hazard. Mater.*, 2012, **219**, 13.
13. D. Liang, C. Cui, H. Hu, Y. Wang, S. Xu, B. Ying, P. Li, B. Lu and H. Shen, *J. Alloys Compd.*, 2014, **582**, 236.
14. J. Liu, H. Bai, Y. Wang, Z. Liu, X. Zhang and D. D. Sun, *Adv. Funct. Mater.*, 2010, **20**, 4175.
15. Q. Li, B. Guo, J. Yu, J. Ran, B. Zhang, H. Yan and J. R. Gong, *J. Am. Chem. Soc.*, 2011, **133**, 10878.
16. G. Xie, K. Zhang, B. Guo, Q. Liu, L. Fang and J. R. Gong, *Adv. Mater.*, 2013, **25**, 3820.
17. C. Chen, W. Cai, M. Long, B. Zhou, Y. Wu, D. Wu and Y. Feng, *ACS Nano*, 2010, **4**, 6425.
18 X.Zhang and Z. chen, *RSC Adv.*, 2015, **5**, 9482.
19. W. S. Hummers and R. E. Offeman, *J. Am. Chem. Soc.*, 1958, **80**, 1339.
20. H. Liu, X. Dong, X. Wang, C. Sun, J. Li and Z. Zhu, *Chem. Eng. J.*, 2013, **230**, 279.
21. H.-i. Kim, G.-h. Moon, D. Monllor-Satoca, Y. Park and W. Choi, *J. Phys. Chem. C*, 2012, **116**, 1535.
22. A. A. Ismail, R. A. Geioushy, H. Bouzid, S. A. Al-Sayari, A. Al-Hajry and D. W. Bahnemann, *Appl. Catal., B*, 2013, **129**, 62.
23. S. Iijima, *Nature*, 1991, **354**, 56.
24. S. Park and R. S. Ruoff, *Nat. Nanotechnol.*, 2009, **4**, 217.
25. P. Solis-Fernandez, J. I. Paredes, S. Villar-Rodil, A. Martinez-Alonso and J. M. D. Tascon, *Carbon*, 2010, **48**, 2657.
26. Y. Xu, H. Bai, G. Lu, C. Li and G. Shi, *J. Am. Chem. Soc.*, 2008, **130**, 5856.
27. Y. Yu, J. C. Yu, C.-Y. Chan, Y.-K. Che, J.-C. Zhao, L. Ding, W.-K. Ge and P.-K. Wong, Appl. Catal., B, 2005, **61**, 1.
28. Y. Lei, L. Zhang and J. Fan, *Chem. Phys. Lett.*, 2001, **338**, 231.
29. K. N. Kudin, B. Ozbas, H. C. Schniepp, R. K. Prud'homme, I. A. Aksay and R. Car, *Nano Lett.*, 2008, **8**, 36.
30. A. C. Ferrari and D. M. Basko, *Nat. Nanotechnol.*, 2013, **8**, 235.
31. K. Li, J. Xiong, T. Chen, L. Yan, Y. Dai, D. Song, Y. Lv and Z. Zeng, *J. Hazard. Mater.*, 2013, **250**, 19.
32. G. Eda and M. Chhowalla, *Adv. Mater.*, 2010, **22**, 2392.
33. G. Jiang, Z. Lin, C. Chen, L. Zhu, Q. Chang, N. Wang, W. Wei and H. Tang, *Carbon*, 2011, **49**, 2693.
34. A. Naldoni, M. Allieta, S. Santangelo, M. Marelli, F. Fabbri, S. Cappelli, C. L. Bianchi, R. Psaro and V. Dal Santo, *J. Am. Chem. Soc.* , 2012, **134**, 7600.
35. B. Li, X. Zhang, X. Li, L. Wang, R. Han, B. Liu, W. Zheng, X. Li and Y. Liu, *Chem. Commun.*, 2010, **46**, 3499.
36. Y. Wang, Y. Hao, H. Cheng, J. Ma, B. Xu, W. Li and S. Cai, *J. Mater. Sci.*, 1999, **34**, 2773.
37. E. S. Kim, N. Nishimura, G. Magesh, J. Y. Kim, J. W. Jang, H. Jun, J. Kubota, K. Domen and J. S. Lee, *J. Am. Chem. Soc.*, 2013, **135**, 5375.
38. J. Cao, B. Xu, H. Lin and S. Chen, *C Chem. Eng. J.*, 2013, **228**, 482.
39. A. Benayad, H. J. Shin, H. K. Park, S. M. Yoon, K. K. Kim, M. H. Jin, H. K. Jeong, J. C. Lee, J. Y. Choi and Y. H. Lee, *Chem. Phys. Lett.*, 2009, **475**, 91.